applied sciences

MDPI

Article

A Route to Selective Arsenate Adsorption in Phosphate Solutions via Ternary Metal Biopolymer Composites

Nam T. Bui, Bernd G. K. Steiger and Lee D. Wilson *

Department of Chemistry, University of Saskatchewan, 110 Science Place, Saskatoon, SK S7N 5C9, Canada; trb161@usask.ca (N.T.B.); bernd.steiger@usask.ca (B.G.K.S.)
* Correspondence: lee.wilson@usask.ca; Tel.: +1-306-966-2961

Abstract: With the increased need for improved adsorbents for efficient water treatment, sodium alginate (NaAlg) and chitosan (Chi) represent promising platform biopolymers for the preparation of biocomposite adsorbents for the effective removal of waterborne oxyanion (arsenate (As_i) and orthophosphate (P_i)) contaminants. The TMCs were characterized by spectroscopy (infrared (IR), SEM with an energy dispersive X-ray (SEM-EDX)), point-of-zero-charge (PZC) measurements, and dye adsorption by employing *p*-nitrophenol at variable pH. Based on dye adsorption results, the adsorbent surface area (SA) was 271 m^2/g for Al-TMC, 286 m^2/g for Fe-TMC, and 311 m^2/g for Cu-TMC. This indicates the role of adsorbent pore structure and swelling in water. Further, the role of either aluminum (Al), copper (Cu), or iron (Fe) for the preparation of TMCs for the selective As_i removal in the presence of P_i as a competitor anion was evaluated. While Al, Fe, and Cu coordinate to the biopolymer framework at C=O sites, only Fe coordinates to $–NH_2$ sites. While Al coordinated via Al-O and interfacial hydroxy groups, Cu showed the formation of $Cu_2(OH)_3NO_3$ in contrast to Fe, which observed FeOOH formation. Adsorption of As_i was highest for Al-TMC (80 mg/g), followed by Fe-TMC (77 mg/g) and Cu-TMC (31 mg/g). Adsorption of P_i was highest for Al-TMC (93 mg/g), followed by Fe-TMC (66 mg/g) and Cu-TMC (17 mg/g). While Al-TMC showed the highest adsorption capacity overall, only Fe-TMC (followed by Cu-TMC) showed strong arsenate selectivity over orthophosphate. The selectivity toward As_i in presence of P_i was determined and the binary separation factor ($\alpha_{t/c}$) and the selectivity coefficient (β_t) were calculated, where Cu-TMC ($\alpha_{t/c}$ = 6.1; β_t = 4.4) and Fe-TMC ($\alpha_{t/c}$ = 8.3; β_t = 5.0) exceeded Al-TMC ($\alpha_{t/c}$ = 1.5; β_t = 1.2). This work contributes to the field of oxyanion-selective adsorbents via judicious selection of the metal salt precursor during the synthetic design of the ternary biocomposite systems, as demonstrated herein.

Keywords: chitosan; alginate; ternary metal composites; arsenate selective adsorption; biopolymers; phosphate removal

check for updates

Citation: Bui, N.T.; Steiger, B.G.K.; Wilson, L.D. A Route to Selective Arsenate Adsorption in Phosphate Solutions via Ternary Metal Biopolymer Composites. *Appl. Sci.* **2024**, *14*, 7577. https://doi.org/10.3390/app14177577

Academic Editors: Andrzej Pacana and Dominika Siwiec

Received: 1 August 2024
Revised: 21 August 2024
Accepted: 23 August 2024
Published: 27 August 2024

Copyright: © 2024 by the authors. Licensee MDPI, Basel, Switzerland. This article is an open access article distributed under the terms and conditions of the Creative Commons Attribution (CC BY) license (https://creativecommons.org/licenses/by/4.0/).

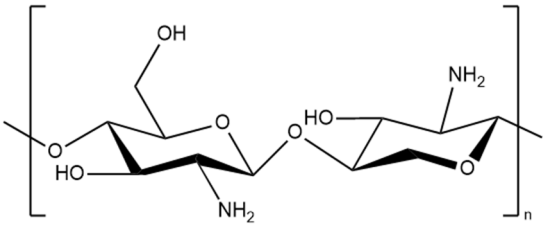
1. Introduction

Over the past decade, industrial and technological developments have transformed the anthrosphere, enabling a breakthrough in productivity. However, these activities may pollute water bodies with various oxyanion contaminants, such as phosphate, arsenate, etc. Arsenate is a well-known carcinogen with a wide range of biological hazards [1]. The ubiquitous occurrence of arsenate is revealed by its contamination in over 70 countries, including Canada, which highlights the global importance of the removal of this waterborne contaminant. Among various water remediation methods such as ion exchange, reverse osmosis, and coagulation-flocculation, adsorption offers flexibility, low cost, low sludge volume, ease of operation, and design advantages [2,3]. Due to these advantages, phosphate and arsenate adsorption processes that employ environmentally friendly materials are attracting significant interest in the field.

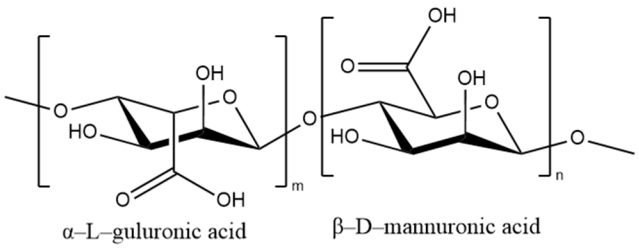
In the environment, two main forms of arsenic are present, in the form of arsenite (As(III)) and arsenate (As(V)) oxyanions. Herein, the focus is on the more prevalent arsenate

species, As(V). Typical arsenate concentrations are below 0.01 mg/L, main tailings and other high arsenate sources may reach up to 5 mg/L (arsenic) [4,5]. However, selective removal of arsenic may present challenges in the presence of co-contaminants such as phosphate, which may occur at elevated concentrations (up to 5 mg/L) in aquatic environments [6–8]. Orthophosphate (P_i), in particular, represents challenges concerning arsenate selectivity based on similar pK_a values (hence, speciation in water), geometry (tetrahedral), and similar Lewis base hardness [9]. Differentiating traits were identified as size and hydration energy, where arsenate is considerably less hydrated than orthophosphate. The competitive effects of phosphate were summarized by Pincus et al., where metal-based adsorbents (Fe, Al, Ti, etc.) for arsenate observed a 10–90% reduction in As_i adsorption capacity in the presence of orthophosphate [9].

For sustainable water remediation, using biopolymer materials becomes ever more important, where two key examples of versatile biopolymers include chitosan (Chi) and alginate (NaAlg). Chitosan is produced by the deacetylation of chitin, a naturally abundant biopolymer found in fungi, shrimp shells, crab shells, and other crustaceans, where its molecular structure is shown in Scheme 1 [10]. By comparison, alginate is a natural polymer found in brown seaweed and bacteria that contain α-L-guluronic and β-D-mannuronic acid monomer units, where its molecular structure is shown in Scheme 2 [11,12]. The abundant functional groups of chitosan (–OH and $–NH_2$), and alginate (–OH and –COOH) represent potential complexation sites for metal centers due to their Lewis base character [13]. The relative abundance of chitosan and alginate and their ability to form biocomposites can offer a unique strategy to generate environmentally friendly and low-cost adsorbents with tunable selectivity and adsorption capacity for oxyanions such as phosphate and arsenate.



Scheme 1. Simplified biopolymer structure of a repeat unit of fully deacetylated chitin, where levels of 50% acetylation at C2 refer to the structure of chitosan.



Scheme 2. Simplified biopolymer structure of a repeat unit of alginic acid.

Kumar et al. demonstrated the utility of chitosan and alginate to form polyelectrolyte complexes that contain Al(III) cations, where alginate binds favourably to the Al(III) cations [14]. The resulting material utilizes the biopolymers as scaffolds for the active metal centers, which function as active adsorption sites. Therein, the composites were able to adsorb a variety of contaminants from organic dyes to chromate oxyanions. This research was extended to the design of sulphate adsorbents by Steiger et al. and further extended to other oxyanions such as arsenate and orthophosphate systems [15–17]. Arsenate adsorption was investigated by employing various aluminum-based ternary metal composites (TMCs), where P_i adsorption was probed with TMCs (and binary metal-composites (BMCs) that contain a metal species and biopolymer building blocks). Various metal species may include Fe, Cu, or Al. The germane findings can be summarised as follows: For P_i adsorption,

it was found that the HSAB principle governs the adsorption mechanism, in contrast to As_i which chemisorbs via ligand exchange (As-O-Al bridging) [18].

The identified knowledge gap in this study was focused on the adsorption properties of the TMCs with arsenate and orthophosphate in binary aqueous solutions in an effort to gain insight into the binding mechanism onto the TMC adsorbents with variable metal centers. We posit that TMCs with variable types of metal ions are anticipated to yield variable arsenate selectivity. To this end, three types of TMC materials were prepared and characterized based on three metal systems (Al-TMC, Fe-TMC, and Cu-TMC). In particular, the IR spectra, PZC measurements, and adsorption equilibrium profiles of these materials with phosphate and arsenate under controlled pH and conditions were investigated to reveal the different metal coordination onto the biopolymer framework. Ion chromatography (IC) was performed to investigate the role of different metal centers on P_i and As_i selectivity and to provide further insight into the overall adsorption mechanisms of the various TMCs. This work contributes to the field of adsorption science and technology since the biocomposites reported herein with variable metal centers lend to the development of adsorbent technology with improved arsenate selectivity over orthophosphate in aqueous media, which is highly relevant to aquatic environmental samples.

2. Materials and Methods

2.1. Materials

Sodium alginate with 12–40 kDa (39% guluronate units, 61% mannuronate units), KBr (FT-IR grade, 99%+), aluminum nitrate nonahydrate (98%+), iron(III) nitrate nonahydrate (98%+), copper(II) nitrate hemi-pentahydrate (98%), glacial acetic acid (ACS, 99.7%) potassium sodium tartrate tetrahydrate (ACS, 99%), Potassium antimony (II) tartrate hydrate (ACS, 99%+), ammonium molybdate (ACS, 81–83%), L-ascorbic acid (ACS), sulfuric acid anhydrous (ACS, 99.9%+) were purchased from Sigma-Aldrich Canada (Oakville, ON, Canada). A vanadate-molybdate reagent (for phosphate determination; ready to use in solution form) was obtained from Sigma-Aldrich Canada (Oakville, ON, Canada). Low molecular weight chitosan (82% deacetylation, 50–190 kDa), potassium phosphate monobasic (ACS), NaOH, and sodium bicarbonate were purchased from Fisher Scientific Chemicals (Fisher Scientific, Ottawa, ON, Canada). Sodium hydrogen arsenate heptahydrate (ACS) and 4-nitrophenol (PNP; purity: 99%), were obtained from Alfa Aesar (Ward Hill, MA, USA). PNP was recrystallized in water before use. All chemicals were used as received unless specified otherwise. Millipore water (18.2 MOhm) was used throughout the preparation of all solutions.

2.2. Synthesis of Ternary Metal Composites (TMCs)

The TMCs were synthesized by dissolving ~1 g of chitosan in 100 mL of 2% acetic acid and alginate (~1 g) in ~100 mL of Millipore water. After the complete dissolution of the biopolymers, the chitosan solution was slowly added to the alginate solution with stirring. After homogenizing at 295 K with stirring, 100 mL of metal nitrate solution (1 M) was slowly added to the chitosan-alginate solution. After homogenizing for ~3 h at 295 K, the pH was raised to ~6.5 by the addition of a 2 M NaOH solution (measured with a Mettler Toledo Seven Compact with an Accumet 13-620-108A electrode, Fisher Scientific, Ottawa, ON, CA). The resulting precipitate was left to settle overnight, followed by filtration, and washing with copious amounts of Millipore water. Afterward, the solids were dried in an oven for ~24 h before grinding the product into a fine powder.

2.3. Characterisation

The FT-IR spectrum for chitosan, alginate, and the synthesized materials were collected using a Bio-Rad-FTS-40 instrument (Bio-Rad Laboratories, Inc., Santa Clara, CA, USA). The samples were collected in a 1:10 (wt. ratio) with IR grade KBr with co-grinding into a fine powder for spectral analysis.

PZC measurements were obtained for Al-TMC, Cu-TMC, Fe-TMC, sodium alginate, and chitosan using the pH-drift method. In brief, 60 mg of sample were added to 25 mL of 0.01 M NaCl (*aq*) with a starting pH ranging between 3 to 8. The NaCl concentration was held constant to ensure consistent sensitivity of the pH meter. After shaking at 298 K for 48 h, the final pH for each solution was measured to plot the change in pH (ΔpH) vs. initial pH [19].

SEM-EDX analysis was carried out on a Hitachi SU8010 Scanning Electron Microscope equipped with 170 mm^2 Ultim max Energy Dispersive Detector from Oxford instruments. All EDX scans were obtained at an operating voltage of 17 kV. AZTEC 4.3 data acquisition software was employed to obtain the EDX patterns.

For the surface area (SA) determination of the TMC materials in their dry state, an ASAP 2020 surface area and porosity analyzer with N_2 as the backfill gas at −196.2 °C (BET surface area determination) was employed. To investigate the surface area or accessible surface area for dye adsorption in water, PNP solutions with variable concentrations ([PNP] = 2 to 16 mM) were used; 10 mg of each adsorbent material was added to 10 mL to shake in glass vials at 23 °C for 24 h. Then, aliquots of supernatant solution were centrifuged for 1 h before absorbance measurements. The uptake of PNP by the TMCs was measured at pH 8.5 (50 mM sodium bicarbonate buffer) and 508 nm [20,21].

2.4. Isotherm Studies

For the P_i or As_i adsorption experiments, 10 mg of each material was added to 10 mL phosphate stock solution with the P_i or As_i concentration ranging from 50 ppm to 500 ppm and 1000 ppm at pH 6.3–6.7. After the samples were shaken at 23 °C for 24 h, the equilibrium P_i concentration in the solution was measured using the acquired vanadate-molybdate reagent, while the As_i concentration was determined via the prepared solution as outlined in the Supplementary Material (SM). After the reaction with the reagent, the solution absorbance was measured using a SPECTRONIC 200E spectrometer (Thermo Scientific, Waltham, MA, USA) at 720 nm for P_i and 900 nm for As_i [22,23].

Q_e was estimated using Equation (1) where Q_e (mg/g) is the equilibrium uptake, C_o (ppm) and C_e (ppm) are the initial and equilibrium anion concentration of the solution, m (g) is the adsorbate weight and V (L) is the solution volume. The Sips model (Equation (2)) was fit to calculate the phosphate isotherm parameters [24].

$$Qe = \frac{(C_0 - C_e) * V}{m} \quad (1)$$

The Sips isotherm is defined by Equation (2), which can account for Langmuir and Freundlich isotherm behaviour under certain limiting conditions [25–27]. When n = 1, the model describes Langmuir behaviour, whereas Freundlich behaviour occurs when $K * C_e^n << 1$. Q_e (mg/g) and C_e (mg/L (or ppm)) represent the equilibrium concentration of adsorbate in the adsorbent phase and the concentration of adsorbate in the liquid phase, respectively. Therefore, the adsorption isotherm parameters will be calculated via the Sips isotherm model in Equation (2). K is the Sips isotherm constant, and n (dimensionless) is an exponent term that provides a measure of the surface heterogeneity of the adsorption sites present on the adsorbent's surface. Particularly, a value of n closer to 1 reflects adsorption onto a homogeneous surface, while deviation away from 1 reflects adsorption onto heterogeneous surface sites [28].

$$Qe = \frac{Q_{max} * K * C_e^n}{1 + K * C_e^n} \quad (2)$$

2.5. Selectivity Studies

To evaluate the uptake selectivity toward arsenate (As_i) in the presence of orthophosphate (P_i), 10 mg adsorbent was combined with 30 mL solution (8-dram vial) and shaken for 24 h at 295 K. The single analyte solutions were ca. 20–23 mg/L of either As_i or P_i,

or their binary mixtures (As_i + P_i). The P_i concentration was determined via ion chromatography (IC). A Thermo Scientific Dionex Integrion HPIC system with a Dionex AS-DV autosampler, a Dionex IonPac AS18 column (4 × 250 mm), and a Dionex ASRS 300 400 suppressor column was used. Eluent was provided via KOH Dionex EGC-KOH II (23 mM) cartridge. Data analysis was performed via Chameleon software. A 7-anion standard mixture (fluoride, chloride, nitrite, nitrate, bromide, sulphate, phosphate) was used, while the As_i concentration was estimated via spectrophotometry [23].

3. Results and Discussion

Herein, the materials were first characterized via complementary techniques with a focus on FT-IR spectroscopy and SEM-EDX in addition to a surface charge determination via point-of-zero-charge estimation. The second section is dedicated to As_i and P_i adsorption studies, where individual isotherm studies were performed to determine the maximum adsorption capacity without the presence of competitive anion. Then, the influence of a competitive anion (P_i) on As_i adsorption was performed to gauge the selectivity toward As_i depending on the Lewis acid present.

3.1. Characterization

The IR spectrum of chitosan, alginate, and the three TMC materials were compared. The expanded IR spectra can be found in Figures S1–S5 in the Supplementary Materials. The presence of various functional groups in biocomposite materials can be characterized by vibrational spectroscopy, as described in other studies [29–31]. Therefore, identifying the appearance or disappearance of IR spectral bands or changes in spectral intensity can be evaluated to ascertain the nature of the bonding within composite materials.

In Figure 1 the IR spectra reveal a characteristic –OH signal at 3500 cm^{-1} from chitosan and alginate, which is also noted for all biocomposite materials. Notably, the strong C=O stretching band in chitosan and alginate near 1660 cm^{-1} was not found in the TMC materials, which indicates that the C=O groups of chitosan and alginate may serve as strong chelation sites for the metal centers [32]. A notable IR signature was attributed to the nitrate counter-ion near 1390 cm^{-1}. The expected signal was observed for Al-TMC and Fe-TMC systems, but was not apparent for Cu-TMC. Instead, the Cu-TMC IR spectrum (cf. Figure 1) exhibits a set of signatures at 3540 cm^{-1}, 2450 cm^{-1}, 2336 cm^{-1}, 1420 cm^{-1}, 1350 cm^{-1}, and 1050 cm^{-1}, which are characteristic spectral features for $Cu_2(OH)_3NO_3$ [33,34], as noted for IR results reported by Steiger and Wilson for a related Cu-TMC biocomposite [32]. This possibly signifies a fundamental difference for copper-based materials, where $Cu_2(OH)_3NO_3$ are formed in the synthesis and may be incorporated within the biopolymer network. While in Al-TMC and Fe-TMC, the metal centers are chelated to the functional groups of the biopolymers in their oxo-coordinated form (Al-O and FeO(OH)) and nitrate simply acts as the counter ion for charge balance [15,16].

3.1.1. Point of Zero Charge Determination

PZC measurements for the Al-, Cu-, and Fe-TMCs were compared with NaAlg and Chi to reveal the effect of different metal centers on the surface chemistry of the materials. The PZC results were obtained by taking the x-intercept of the change in pH vs. the initial pH plot (see Table 1), where the PZC of chitosan was higher than the TMCs or NaAlg.

Table 1. Point-of-zero-charge (PZC) results for TMCs and precursor materials.

Materials	PZC
Al-TMC	4.7
Cu-TMC	5.6
Fe-TMC	5.1
NaAlg	6.6
[a] Chi	8.4

Note: [a] The PZC was obtained from Ref. [17].

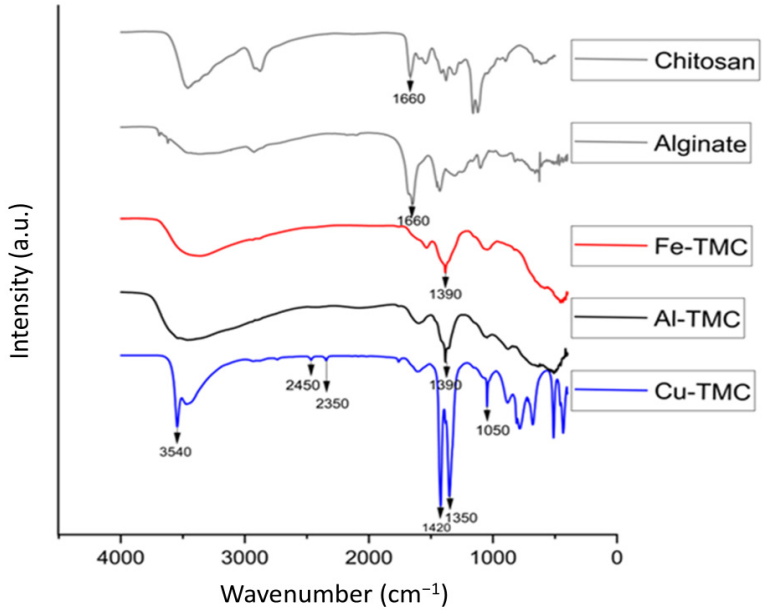


Figure 1. IR spectra of Alginate, Chitosan, and TMC materials before adsorption.

The incorporation of a metal center into the biopolymer framework resulted in a decrease in the point-of-zero charge (PZC), with the Al-TMC being the lowest, followed by Fe-TMC, and finally Cu-TMC with the highest value. The decreasing order of PZC values with Lewis acid strength suggests a direct relationship between the metal speciation and the surface charge of TMCs [9,16]. With Al being the stronger Lewis acid, the PZC of the Al-TMC was shown to be the lowest. Conversely, Cu(II) is the weakest Lewis acid among the three systems, which can account for Cu-TMC having the highest PZC or lowest surface charge. Combined with the isotherm profiles of the TMC materials, a strong correlation between the surface charge of the materials and adsorption capacity may be established.

3.1.2. SEM-EDX Analysis

A crucial factor in the analysis of the prepared TMC material is the composition and elemental distribution within the sample matrix. Elemental analysis via EDX mapping estimation of the composition of a sample spot, but also to visualize the elemental distribution (homogeneous vs. heterogeneous) across the sample region. Several regions of the sample (n = 5) were analyzed, as shown in Figures S16–S49 in the Supplementary Materials, where selected sample images are presented. However, based on the instrumental limitations, the quantification of N is semi-quantitative due to the significant overlap between the N and C Kα line, especially at low N concentrations. In contrast, the mapped images for the elemental distribution may show nitrogen. The average composition for each sample type is listed in Table 2.

The elemental quantification and mapping were focused on the metal centers, hence, small deviations in the determined wt.% due to Kα overlap of C and N may be less significant compared to samples without metal content. The average composition (wt.%) detected via EDX mapping is broadly corroborated by X-ray photoelectron spectroscopy (XPS) performed in an earlier study for various composites [17]: Al-TMC with ca. 31 wt.% Al and 52 wt.% O; Cu-TMC with 35 wt.% Cu and 42 wt.% O; Fe-TMC with 48 wt.% Fe and 33 wt.% O. Therein, Al-TMC was found to have 1.75 wt.% N, while Fe-TMC contained ca. 1.44 wt.% N. The high N content in Cu-TMC with 4.63 wt.% agrees with the EDX quantification. (cf. Table S3 in the Supplementary Materials of [17]). Specific to Al-TMC is the mostly homogeneous composition across multiple sampling spots with an average of 59 wt.% oxygen and 25 wt.% aluminum. This trend is congruent with most of the Al-O-species coordinated onto the biopolymer framework, and also indicates considerable metal content in the TMCs. Cu-TMC shows a similar trend, except for increased N content

due to the formation of $Cu_2(OH)_3(NO_3)$ salts. Fe-TMC, on the other hand, shows mostly heterogeneous composition within the composite, with areas rich or deficient in Fe. It can therefore be estimated that at least 2–5 wt.% N must be present for detection and the appropriate wt.% needs to be removed from C for a more accurate elemental quantification.

Table 2. The average composition of the three prepared TMCs.

	Al-TMC (wt.%)	Cu-TMC (wt.%)	Fe-TMC (wt.%) *
O	59 ± 3	40 ± 3	35 ± 15
Al	25 ± 4	N/A	N/A
C	15 ± 2	12 ± 1	13 ± 3
N	0 **	5 ± 1 **	1 ± 2 **
Cu	N/A	42 ± 4	N/A
Fe	N/A	N/A	48 ± 20
Na	0	0	2 ± 3

Note: * Large standard deviation resulted from spots with vastly different elemental composition (e.g., Spot 1 with 76 wt.% Fe and 13 wt.% O vs. Spot 5 with 25 wt.% Fe and 49 wt.% O); N/A: Not applicable. ** Inaccurate at low concentrations due to overlap with C.

The use of SEM-EDX results provides additional information like elemental distribution and surface imaging. For Al-TMC, one exemplary spot is shown in Figure 2.

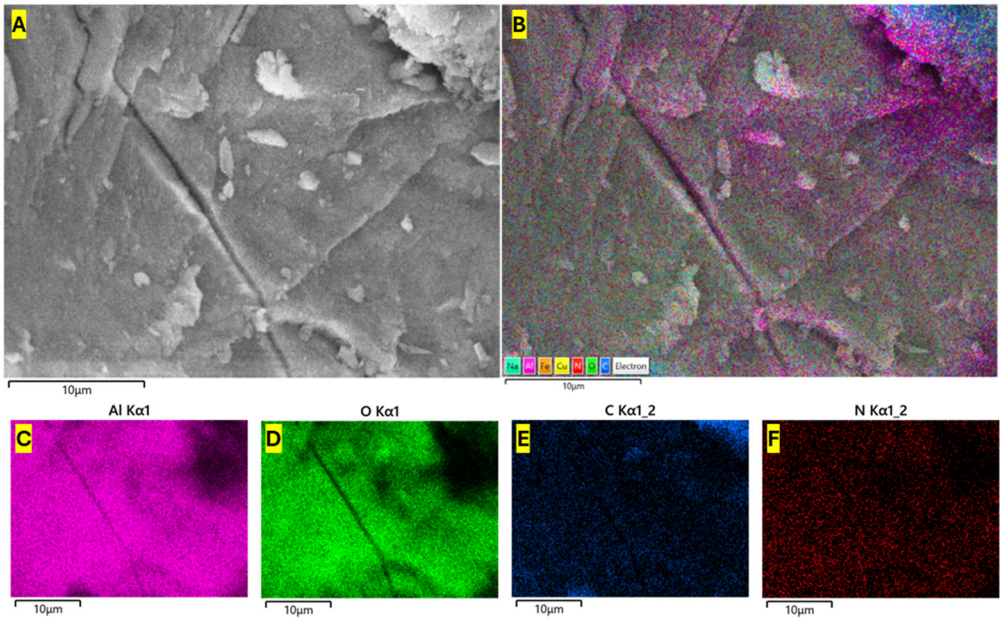


Figure 2. SEM-EDX analysis of Al-TMC, (**A**) electron Image without mapping, (**B**) compositional mapping, (**C**–**F**) elemental distribution for Al, O, C, and N.

Further to the inhomogeneity of the Al distribution, which aligns with the O distribution that is indicative of Al-O coordination, a mainly smooth surface of the particles was detected. The low N content may indicate that the metal oxide particles are mostly on the surface of the composite. In contrast, Cu-TMC observes a more particle-laden, rough surface morphology, in addition to homogeneous Cu elemental distribution (cf. Figure 3).

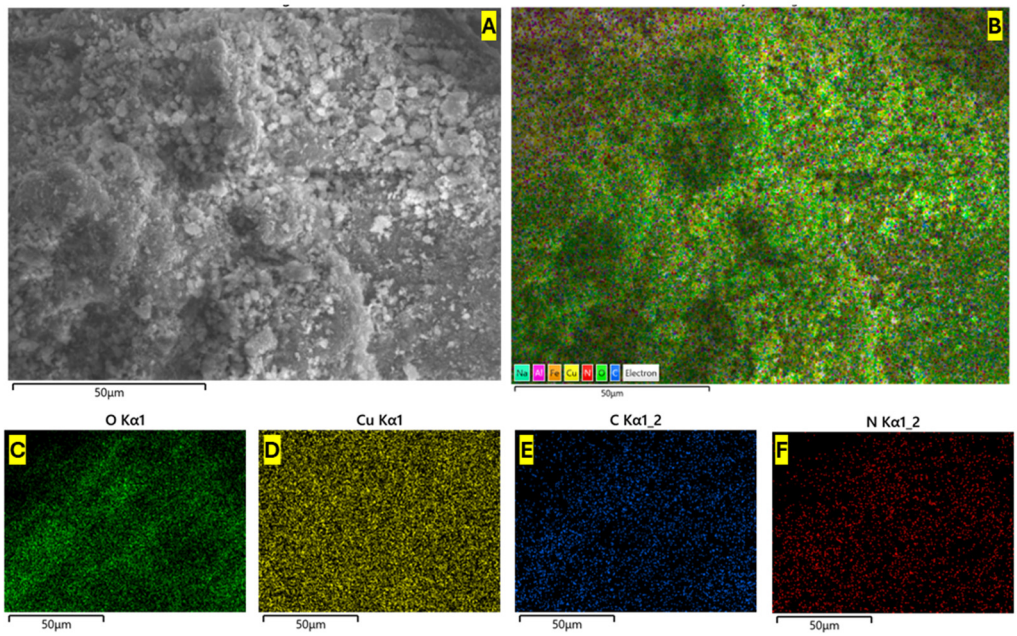


Figure 3. SEM-EDX analysis of Cu-TMC, (**A**) electron image without mapping, (**B**) computational mapping, (**C**–**F**) elemental distribution for O, Cu, C, and N.

The spatial overlap between O, N, and C provides evidence for the presence of the biopolymer framework, whereas Cu is evenly distributed across the framework. The elemental composition for Fe-TMC showed, in contrast to both Al-TMC and Cu-TMC, increased sample inhomogeneity (cf. Table 2). This is further illustrated by SEM-EDX mapping of different sample spots in Fe-TMC (cf. Figure 4).

A more homogeneous distribution of Fe on the seemingly more porous biocomposite surface was observed in Figure 4A, in contrast to the O-distribution (cf. Figure 4C). The second sample spot revealed a "smooth" surface (Figure 4F) with mostly O-content in conjunction with C, in addition to "veins" of Fe on the surface. The elevated presence of C, N, and O indicated a more biopolymer-rich framework on the surface, in contrast to spot 1 (Figure 4A). This may indicate that the mixing process for the Alg and Chi solutions for PEC formation could introduce small inaccessible regions where subsequently lower Fe-association occurs, which gives rise to a "smoother" surface appearance with different Fe-distribution compared to other spots.

3.2. Adsorption Isotherms

The phosphate isotherm parameters are summarized in Table 3, whereas the arsenate isotherm parameters are summarized in Table 3 (see also Figures S7–S15 in Supplementary Materials for the As_i and P_i isotherms).

Table 3. Best-fit Sips isotherm parameters (cf. Equation (2)) for P_i adsorption at pH 6.3 at 23 °C.

Adsorbent	Al-TMC	Fe-TMC	Cu-TMC
Q_{max} (mg/g)	93	77	17
K	0.90	0.28	0.36
n	0.82	0.28	1.2

Overall, Al-TMC has the highest adsorption capacity for both P_i and As_i. This can be explained by the higher charge density at the Al center and the lower PZC of Al-TMC. The n-value of the Sips model for both Al-TMC and Cu-TMC approaches unity and indicates multiple binding sites for Fe-TMC (*n*-value of ca. 0.3) while mostly homogeneous binding for the other composites is indicated.

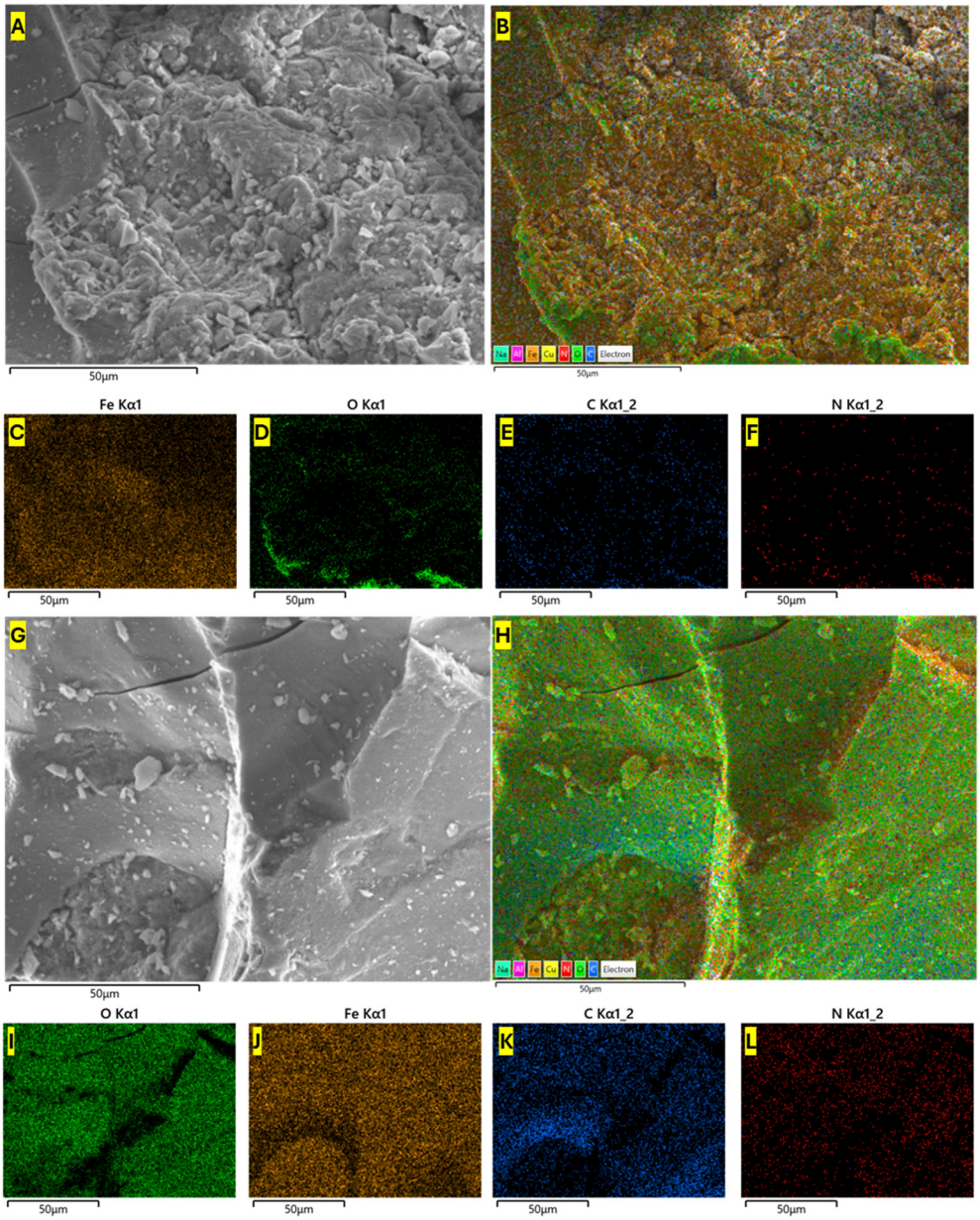


Figure 4. SEM-EDX analysis of Fe-TMC, (**A**) electron Image without mapping, (**B**) compositional mapping, (**C**–**F**) elemental distribution for Fe, O, C, and N of spot 1, and (**G**) electron Image without mapping, (**H**) compositional mapping, (**I**–**L**) elemental distribution for Fe, O, C, and N of spot 2.

The isotherm data for As_i reveals a deviation of the heterogeneity factor (n) away from unity ($n \neq 1$) for all materials that reflect heterogeneous binding sites for the biocomposites. In summary, Table 4 lists the monolayer equilibrium adsorption capacity (Q_m; mmol/g) of both As_i and P_i for direct comparison, while Table 5 lists the adsorption capacity in mmol/g.

Table 4. Best-fit Sips isotherm parameters (cf. Equation (2)) for As_i adsorption at pH 6.7 at 23 °C.

Adsorbent	Al-TMC	Fe-TMC	Cu-TMC
Q_{max} (mg/g)	80	66	31
K	14.7	0.57	2.58×10^{-5}
n	0.18	0.38	2.72

Table 5. Adsorption capacity (Q_e) of arsenate (140 g/mol) versus orthophosphate (97 g/mol) at pH 6.3–6.7.

	Al-TMC	Fe-TMC	Cu-TMC
Orthophosphate (mmol/g)	0.96	0.79	0.18
Arsenate (mmol/g)	0.57	0.47	0.22

For the case of adsorption capacity expressed as molar units (mmol/g) (cf. Table 5), the uptake for Al-TMC toward P_i is ca. 70% higher compared to As_i, and similar to the Fe-TMC. By comparison, Cu-TMC shows similar adsorption capacities for both As_i and P_i.

3.3. Accessible Surface Area Determination

The surface area of adsorbents can be measured via nitrogen gas adsorption isotherms (via BET) and compared to both the starting materials and a variety of powdered adsorbents. However, gas adsorption provides limited information concerning the porosity and available surface area for cases when the adsorbent undergoes swelling in aqueous media. To evaluate the accessible surface area (SA) for anion adsorption in a liquid medium, PNP adsorption isotherms were obtained at pH 8.5, and analyzed via the Sips model to obtain Q_e. At this pH, PNP is deprotonated since the pH lies above the pK_a of PNP (ca. 7.2) and approximates an oxyanion species with a single negative charge. A noticeable feature of the PNP isotherms is that Cu-TMC reveals greater SA versus the Al and Fe-TMC materials, according to the dye adsorption method. It is expected that PNP exists in its nonionized phenol form at pH 6.3–6.7, where the role of potential metal cation-π interactions occur, in addition to London dispersion forces between the dye and biopolymer framework. This contrasts with the adsorption of inorganic oxy-anions that involve anion-cation interactions (metal cation-oxyanion). At pH 8.5, the phenolate form of PNP prevails and additional contributions due to phenolate-metal ion interactions may prevail, which is supported by the systematically higher Q_e and SA values at alkaline pH conditions, as revealed in Table 6.

Table 6. Surface area (SA) determination via isotherm parameters fit with the Sips model for PNP adsorption at pH 8.5 (wet state) and comparison with the measured BET surface area (dry state).

Adsorbent	Al-TMC	Fe-TMC	Cu-TMC
Q_e (mmol/g)	1.52	2.03	2.06
K	0.11	0.14	0.52
n	8.62	4.69	2.5
SA PNP (m^2/g)	271	286	311
SA BET (m^2/g)	1.59	70.2	30.5

For comparison, the BET surface area of NaAlg was measured as 1.46 m^2/g, and that of Chi as 1.06 m^2/g. While Al-TMC observed a similar SA in its dry state compared to NaAlg or Chi, Cu-TMC showed almost a 30-fold increase in its SA, after Fe-TMC with a SA of 70 m^2/g. For the adsorption properties, however, it is germane to include solvent swelling and increased access to surface adsorption sites, hence PNP adsorption isotherms were determined. Although the magnitude of the SA values of all composites are similar, the SA estimated for Cu-TMC was the highest, followed by Fe-TMC, and the lowest for Al-TMC. The isotherms of PNP adsorption at pH 8.5 are shown in Figure 5. This corroborates the observations made for SEM-EDX mapping, where a more porous appearance (Cu-TMC and Fe-TMC) is reflected in a drastically increased (dry) SA compared to Al-TMC. In addition, the discrepancy between the N2 gas BET estimate and the PNP dye estimate indicates that the SA in the dry state does not reflect the relative adsorption capacity toward the oxyanions, due to solvent swelling effects because of variable surface chemical and porosity effects.

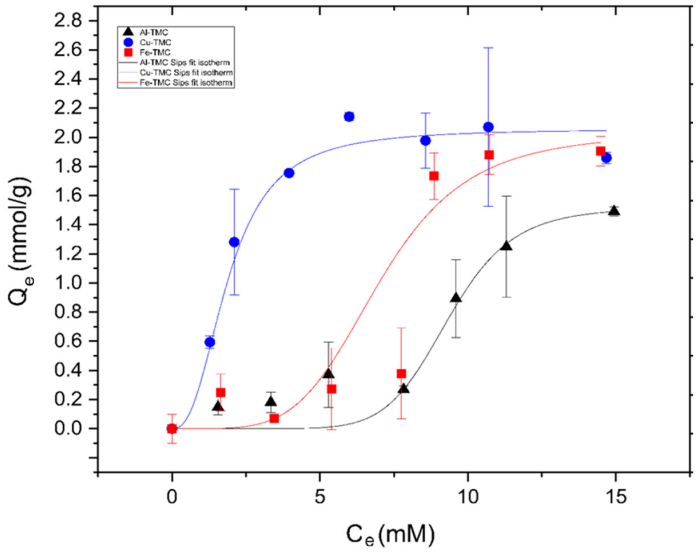


Figure 5. PNP adsorption isotherms with various TMCs at pH 8.5.

In addition to the dye-based SA determination via PNP in an aqueous environment, the binding mechanism was examined via IR spectral results that consider a potential anion exchange mechanism.

As shown in Figure 6, the disappearance of the 1390 cm^{-1} signals in Al-TMC and Fe-TMC indicates the displacement of nitrate counter ions, supporting the role of the PNP anion at pH 8.5, as compared to the neutral dye species at slightly acidic conditions (ca. pH 6.3–6.7). The increasing sharpness of the -OH signal near 3500 cm^{-1} also indicates a decrease in hydrogen bonding of the biopolymers.

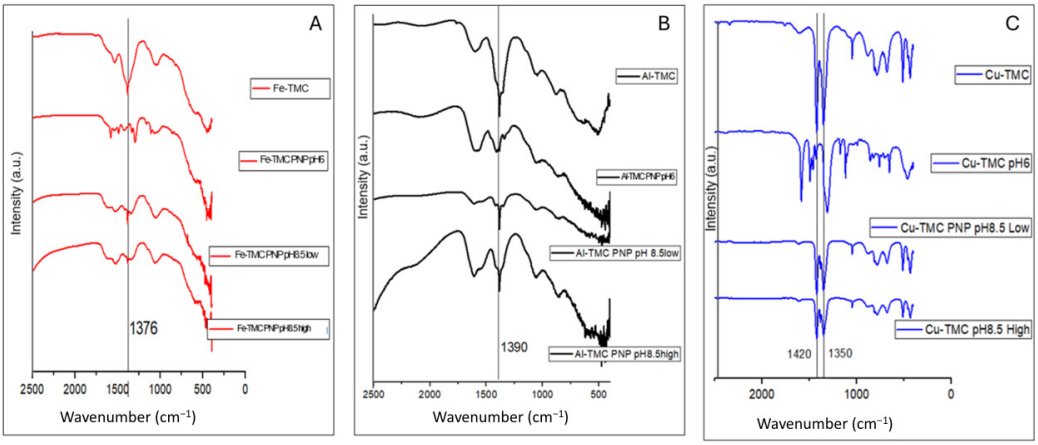


Figure 6. IR spectra for Fe-TMC (**A**), Al-TMC (**B**), and Cu-TMC (**C**) before and after PNP adsorption at pH 6, pH 8.5 low concentration, and pH 8.5 high concentration.

3.4. Arsenate to Phosphate (As_i/P_i) Adsorption-Based Selectivity

To determine the selectivity of an adsorbent toward a target adsorbate species, a variety of methods can be used. The adsorption capacities of both As_i and P_i in a mixed system are shown in Figure 7.

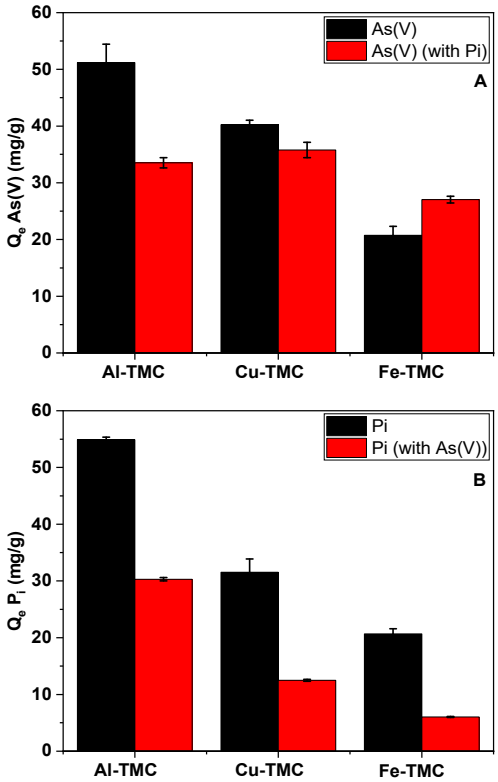


Figure 7. Selectivity studies on all three TMCs with phosphate (P_i) alone (**B**), arsenate (As_i) alone (**A**), and their mixtures (P_i + As_i), where the initial concentrations are ca. 20 mg/L.

An often-used factor is percent removal (R; %) due to its wide comparability across different studies in the literature. However, this parameter does not adequately describe the adsorbent efficiency or required dosage. This can be addressed by the incorporation of q (target equilibrium adsorption capacity). Herein, three different selectivity metrics in the form of the adsorption capacity ratio, the binary separation factor ($\alpha_{t/c}$), and the selectivity coefficient β_t were used. The adsorption capacity ratio (AC) can be calculated by employing Equation (3) [9]:

$$\text{adsorption capacity ratio} = \frac{q_t}{q_{(t+c)}} \tag{3}$$

q_t represents the equilibrium adsorption capacity for the target species, while q_{t+c} is the equilibrium adsorption capacity of the target species in the presence of a competitor ion species.

The calculation of $\alpha_{t/c}$ is shown in Equation (4), [9]:

$$\alpha_{\left(\frac{t}{c}\right)} = \frac{q_t C_{e,c}}{q_c C_{e,t}} \tag{4}$$

where q_c is the equilibrium adsorption capacity of the competitor oxyanion species, $C_{e,c}$ is the equilibrium concentration of the competitor oxyanion species, and $C_{e,t}$ is the equilibrium concentration of the competitor oxyanion.

The selectivity coefficient β_t can be calculated from the distribution coefficients $K_{d,t}$ and $K_{d,c}$ as shown in Equations (5) and (6), [9]:

$$K_{d,x} = \frac{C_0 - C_e}{C_e} * \left(\frac{v}{m}\right) \tag{5}$$

$$\beta_t = \frac{K_{d,t}}{K_{d,c}} \tag{6}$$

where $K_{d,x}$ represents either the distribution coefficient $K_{d,t}$ or $K_{d,c}$. C_0 is the initial concentration of an oxyanion species in a mixture (competitive ion present), while C_e represents the equilibrium concentration within a mixture, v refers to the volume (mL) and m is the adsorbent weight (mg). The results for the adsorption capacity ratio, the binary selectivity factor $\alpha_{t/c}$, and the selectivity coefficient β_t are shown in Table 7.

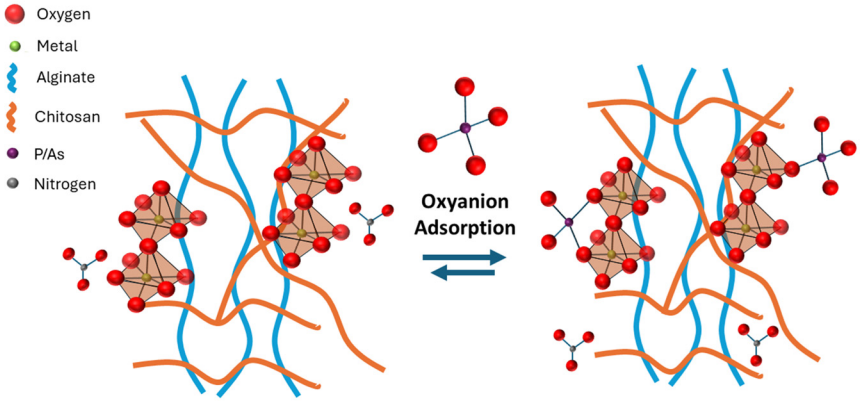
Table 7. Selectivity for arsenate is calculated via concentration (mg/L) and for adsorption capacity (mg/g) for the adsorption capacity ratio, binary selectivity factor $\alpha_{t/c}$, and selectivity coefficient, β_t.

	AC	$\alpha_{t/c}$	β_t
Al-TMC	1.5 ± 0.1	1.5 ± 0.1	1.2 ± 0.1
Cu-TMC	1.1 ± 0.1	6.1 ± 0.7	4.4 ± 0.6
Fe-TMC	0.8 ± 0.1	8.3 ± 0.4	5.0 ± 0.3

In a study of the selectivity of arsenate toward the different TMCs, it was shown that while all materials preferentially adsorb arsenate over phosphate, the Al-TMC observed the lowest selectivity among the biocomposites. Both Cu-TMC and Fe-TMC showed considerably higher arsenate selectivity with Fe-TMC surpassing Cu-TMC (cf. Figure 4).

Whereas the Sips isotherm parameters suggest heterogeneous binding sites for both As_i and P_i, this trend can be explained through hydrogen bonding toward the biopolymer backbone, but mainly due to ligand exchange (especially for Al-TMC and Fe-TMC). In the case of iron-based materials, it has been reported that phosphate can be used to exchange for arsenate, which accounts for the high selectivity of Fe-TMC toward P_i [35,36].

Further, it has been reported that Al-based materials exhibit competitive P_i adsorption, thus revealing a reduced As_i uptake in the presence of P_i [8,37]. In the case of copper (i.e., cupric oxides) TMCs, a tendency for As(V) selectivity over P_i has been observed. In this case, inner sphere complexation was suggested, in addition to electrostatic interactions. However, the mechanism is not fully understood currently [38,39] and Scheme 3 shows a simplified adsorbate-adsorbent interaction for a generic TMC-oxyanion system.



Scheme 3. Simplified illustration of inner sphere coordination of arsenate or phosphate with the active metal complexes of the TMCs.

In summary, the coordination of oxyanions via inner sphere complexation and relative binding strength may give rise to the observed As_i selectivity of Cu-TMC and Fe-TMC, as compared to Al-TMC. While the binding mechanism is posited to occur via inner sphere complexation, the formulae for FeOOH and $Cu_2(OH)_3(NO_3)$ may not lend themselves for ready visualization. To gain a better view, the crystal structure of $Cu_2(OH)_3(NO_3)$ was reported by Ramesh and Madhu, whereas the crystal structure of FeOOH was reported by Issmaeli et al. [40,41].

4. Conclusions

In this study, TMCs with either Fe, Cu, or Al metal centers were prepared and characterized using complementary methods. The IR spectra confirm the role of coordination of Al and Fe onto the biopolymer framework in the form of Al-O and FeOOH species. In contrast, Cu was complexed as $Cu_2(OH)_3NO_3$. Among the three types of metal centers, Fe coordinates with -NH_2 groups of the biopolymer framework, whereas Al and Cu systems do not show such coordination. Examination of the adsorption isotherms for these materials with phosphate and arsenate revealed more apparent and significant differences between the materials. The adsorption capacity of Al-TMC with P_i (93 mg/g) and As_i (80 mg/g) exceeded that for both oxyanions with Fe-TMC (P_i, 77 mg/g and As_i, 66 mg/g) and Cu-TMC (P_i, 17 mg/g and As_i, 31 mg/g). The predominant adsorption mechanism was ligand exchange (inner sphere complexation) of both oxyanions toward the metal centers, with Cu-TMC observing ligand exchange for arsenate adsorption. The selectivity studies further showed that Cu-TMC and Fe-TMC both are significantly more anion-selective toward arsenate ($\alpha_{t/c}$ ca. 6.1 and 8.3 respectively; β_t ca. 4.4 and 5.0, respectively) versus Al-TMC ($\alpha_{t/c}$ ca. 1.5 and β_t ca. 1.2) over orthophosphate. The results of this research are anticipated to contribute to the further development of sustainable biocomposite adsorbents with enhanced arsenate selectivity, even in the presence of the strongly competitive P_i oxyanion species. Thus, the ability to distinguish arsenate from phosphate will serve to address global water security challenges related to arsenic contamination in aquatic environments that co-exist with orthophosphate.

Supplementary Materials: The following supporting information can be downloaded at https://www.mdpi.com/article/10.3390/app14177577/s1, Figure S1: FT-IR spectrum of Al-TMC; Figure S2: FT-IR spectrum of Fe-TMC; Figure S3: FT-IR spectrum of Cu-TMC; Figure S4: FT-IR spectrum of Chitosan; Figure S5: FT-IR spectrum of Sodium Alginate; Figure S6: Change in pH vs initial pH plot; Figure S7: Phosphate adsorption at pH 6.3 isotherm of Al-TMC; Figure S8: Phosphate adsorption at pH 6.3 isotherm of Fe-TMC; Figure S9: Phosphate adsorption at pH 6.3 isotherm of Cu-TMC; Figure S10: Arsenate adsorption isotherm of Al-TMC; Figure S11: Arsenate adsorption isotherm of Fe-TMC; Figure S12: Arsenate adsorption isotherm of Al-TMC; Figure S13: Phosphate adsorption at pH 8.5 isotherm of Al-TMC; Figure S14: Phosphate adsorption isotherm at pH 8.5 isotherm of Fe-TMC; Figure S15: Phosphate adsorption at pH 8.5 isotherm of Cu-TMC; Figure S16: SEM-EDX mapping of Al-TMC (spot 1); Figure S17: Surface morphology and elemental composition of Al-TMC (spot 1); Figure S18: SEM-EDY mapping of Al-TMC (spot 2); Figure S19: Surface morphology and elemental composition of Al-TMC (spot 2); Figure S20: SEM-EDX mapping of Al-TMC (spot 3); Figure S21: Surface morphology and elemental composition of Al-TMC (spot 3); Figure S22: SEM-EDX mapping of Al-TMC (spot 4); Figure S23: Surface morphology and elemental composition of Al-TMC (spot 4); Figure S24: SEM-EDX mapping of Al-TMC (spot 5); Figure S25: Surface morphology and elemental composition of Al-TMC (spot 5); Figure S26: SEM-EDX mapping of Al-TMC (spot 6); Figure S27: Surface morphology and elemental composition of Al-TMC (spot 6); Figure S28: SEM-EDX mapping of Cu-TMC (spot 2); Figure S29: Surface morphology and elemental composition of Cu-TMC (spot 2); Figure S30: SEM-EDX mapping of Cu-TMC (spot 3); Figure S31; Surface morphology and elemental composition of Cu-TMC (spot 3); Figure S32: SEM-EDX mapping of Cu-TMC (spot 4); Figure S33: Surface morphology and elemental composition of Cu-TMC (spot 4); Figure S34: SEM-EDX mapping of Cu-TMC (spot 5); Figure S35: Surface morphology and elemental composition of Cu-TMC (spot 5); Figure S36: SEM-EDX mapping of Cu-TMC (spot 6); Figure S37: Surface morphology and elemental composition of Cu-TMC (spot 6); Figure S38: SEM-EDX mapping of Cu-TMC (spot 7); Figure S39: Surface morphology and elemental composition of Cu-TMC (spot 7); Figure S40: SEM-EDX mapping of Fe-TMC (spot 1); Figure S41: Surface morphology and elemental composition of Fe-TMC (spot 1); Figure S42: SEM-EDX mapping of Fe-TMC (spot 2); Figure S43: Surface morphology and elemental composition of Fe-TMC (spot 2); Figure S44: SEM-EDX mapping of Fe-TMC (spot 3); Figure S45: Surface morphology and elemental composition of Fe-TMC (spot 3); Figure S46: SEM-EDX mapping of Fe-TMC (spot 4); Figure S47: Surface morphology and elemental composition of Fe-TMC (spot 4); Figure S48: SEM-EDX mapping of Fe-TMC (spot 5); Figure S49: Surface morphology and elemental composition of Fe-TMC (spot 5); Table S1: Results of the pH measurements to determine the PZC; Table S2: Tables of ΔpH values and initial pH values used for PZC calculations; Table S3: Isotherm

parameters fit with Sips model for phosphate adsorption at pH 6.3; Table S4: Isotherm parameters fit with Sips model for arsenate adsorption at pH 6.7; Table S5: Isotherm parameters fit with Sips model for arsenate adsorption at pH 8.5.

Author Contributions: Conceptualization: L.D.W.; methodology: B.G.K.S. and L.D.W.; investigation: N.T.B. and B.G.K.S.; data curation: N.T.B.; writing—original draft preparation: N.T.B.; writing—review and editing: B.G.K.S., L.D.W. and N.T.B.; supervision: L.D.W.; funding acquisition: L.D.W. All authors have read and agreed to the published version of the manuscript.

Funding: This research was funded by the Government of Canada through the Natural Sciences and Engineering Research Council of Canada (NSERC) in the form of a discovery grant (RGPIN 04315-2021) to LDW. The Saskatchewan Structural Sciences Centre (SSSC) is acknowledged for providing facilities to conduct this research. Moreover, funding came from the Canada Foundation for Innovation, NSERC, and the University of Saskatchewan to support research at the SSSC. The APC was funded by the MDPI editorial office of Applied Sciences.

Institutional Review Board Statement: Not applicable.

Informed Consent Statement: Not applicable.

Data Availability Statement: Data for this article are provided in the manuscript and the Supporting Material. Further inquiries can be made to the corresponding author.

Acknowledgments: The authors acknowledge that this work was carried out in Treaty 6 Territory and the Homeland of the Métis. As such, we pay our respects to the First Nations and Métis ancestors of this place and reaffirm our relationship with one another. NB acknowledges that this work was conducted under the guidance of LDW and BGKS. Moreover, NB expresses his appreciation toward LDW, BGKS, and Deysi J. Venegas-Garcia for their helpful discussions, support, and feedback throughout this research.

Conflicts of Interest: The authors declare no conflicts of interest.

References

1. Wang, H.; Zhu, H. A Comparison Study on the Arsenate Adsorption Behavior of Calcium-Bearing Materials. *Materials* **2019**, *12*, 1936. [CrossRef]
2. Iwuozor, K.O.; Ighalo, J.O.; Emenike, E.C.; Ogunfowora, L.A.; Igwegbe, C.A. Adsorption of Methyl Orange: A Review on Adsorbent Performance. *Curr. Res. Green Sustain. Chem.* **2021**, *4*, 100179. [CrossRef]
3. Teh, C.Y.; Budiman, P.M.; Shak, K.P.Y.; Wu, T.Y. Recent Advancement of Coagulation–Flocculation and Its Application in Wastewater Treatment. *Ind. Eng. Chem. Res.* **2016**, *55*, 4363–4389. [CrossRef]
4. Wang, S.; Mulligan, C.N. Occurrence of Arsenic Contamination in Canada: Sources, Behavior and Distribution. *Sci. Total Environ.* **2006**, *366*, 701–721. [CrossRef] [PubMed]
5. Astles, B.C.; Chételat, J.; Palmer, M.J.; Vermaire, J.C. Experimental Investigation of Short-Term Warming on Arsenic Flux from Contaminated Sediments of Two Well-Oxygenated Subarctic Lakes. *PLoS ONE* **2022**, *17*, e0279412. [CrossRef]
6. McGinn, P.J.; Park, K.C.; Robertson, G.; Scoles, L.; Ma, W.; Singh, D. Strategies for Recovery and Recycling of Nutrients from Municipal Sewage Treatment Effluent and Hydrothermal Liquefaction Wastewaters for the Growth of the Microalga *Scenedesmus* Sp. AMDD. *Algal Res.* **2019**, *38*, 101418. [CrossRef]
7. Waiser, M.J.; Tumber, V.; Holm, J. Effluent-Dominated Streams. Part 1: Presence and Effects of Excess Nitrogen and Phosphorus in Wascana Creek, Saskatchewan, Canada. *Environ. Toxicol. Chem.* **2011**, *30*, 496–507. [CrossRef]
8. Youngran, J.; Fan, M.; Van Leeuwen, J.; Belczyk, J.F. Effect of Competing Solutes on Arsenic(V) Adsorption Using Iron and Aluminum Oxides. *J. Environ. Sci.* **2007**, *19*, 910–919. [CrossRef]
9. Pincus, L.N.; Rudel, H.E.; Petrović, P.V.; Gupta, S.; Westerhoff, P.; Muhich, C.L.; Zimmerman, J.B. Exploring the Mechanisms of Selectivity for Environmentally Significant Oxo-Anion Removal during Water Treatment: A Review of Common Competing Oxo-Anions and Tools for Quantifying Selective Adsorption. *Environ. Sci. Technol.* **2020**, *54*, 9769–9790. [CrossRef]
10. Ahmed, S.; Ikram, S. (Eds.) *Chitosan*; John Wiley & Sons, Inc.: Hoboken, NJ, USA, 2017; ISBN 9781119364849.
11. Rosiak, P.; Latanska, I.; Paul, P.; Sujka, W.; Kolesinska, B. Modification of Alginates to Modulate Their Physic-Chemical Properties and Obtain Biomaterials with Different Functional Properties. *Molecules* **2021**, *26*, 7264. [CrossRef]
12. Lee, K.Y.; Mooney, D.J. Alginate: Properties and Biomedical Applications. *Prog. Polym. Sci.* **2012**, *37*, 106–126. [CrossRef]
13. Zeng, J.; Qi, P.; Wang, Y.; Liu, Y.; Sui, K. Electrostatic Assembly Construction of Polysaccharide Functionalized Hybrid Membrane for Enhanced Antimony Removal. *J. Hazard. Mater.* **2021**, *410*, 124633. [CrossRef]
14. Kumar, A.; Paul, P.; Nataraj, S.K. Bionanomaterial Scaffolds for Effective Removal of Fluoride, Chromium, and Dye. *ACS Sustain. Chem. Eng.* **2017**, *5*, 895–903. [CrossRef]

15. Steiger, B.G.K.; Udoetok, I.A.; Faye, O.; Wilson, L.D. Counterion Effects in Metal Hybrid Biopolymer Materials for Sulfate Adsorption: An Experimental and Computational Study. *ACS Appl. Polym. Mater.* **2021**, *3*, 9–4595. [CrossRef]
16. Steiger, B.G.K.; Wilson, L.D. Sustainable Hybrid Biocomposite Adsorbents for Anion-Selective or Concerted Removal of Ionic Pollutants: Organic Dyes to Arsenate. *J. Clean. Prod.* **2023**, *422*, 138616. [CrossRef]
17. Steiger, B.G.K.; Wilson, L.D. Biopolymer-Metal Composites for Selective Removal and Recovery of Waterborne Orthophosphate. *Chemosphere* **2023**, *349*, 140874. [CrossRef] [PubMed]
18. Miedaner, M.M.; Weerasooriya, R.; Tobschall, H.J. Chapter 17—1-PK Modeling Strategies for the Adsorption of Some Trace Elements onto Gibbsite. *Interface Sci. Technol.* **2006**, *11*, 469–490.
19. Yang, Y.; Chun, Y.; Sheng, G.; Huang, M. PH-Dependence of Pesticide Adsorption by Wheat-Residue-Derived Black Carbon. *Langmuir* **2004**, *20*, 6736–6741. [CrossRef]
20. Chalil Oglou, R.; Gokce, Y.; Yagmur, E.; Aktas, Z. Production of Demineralised High Quality Hierarchical Activated Carbon from Lignite and Determination of Adsorption Performance Using Methylene Blue and P-Nitrophenol: The Role of Surface Functionality, Accessible Pore Size and Surface Area. *J. Environ. Manag.* **2023**, *345*, 118812. [CrossRef]
21. Steiger, B.G.K.; Wilson, L.D. Modular Chitosan-Based Adsorbents for Tunable Uptake of Sulfate from Water. *Int. J. Mol. Sci.* **2020**, *21*, 7130. [CrossRef]
22. Ibnul, N.K.; Tripp, C.P. A Simple Solution to the Problem of Selective Detection of Phosphate and Arsenate by the Molybdenum Blue Method. *Talanta* **2022**, *238*, 123043. [CrossRef] [PubMed]
23. Okazaki, T.; Kuramitz, H.; Hata, N.; Taguchi, S.; Murai, K.; Okauchi, K. Visual Colorimetry for Determination of Trace Arsenic in Groundwater Based on Improved Molybdenum Blue Spectrophotometry. *Anal. Methods* **2015**, *7*, 2794–2799. [CrossRef]
24. Wang, J.; Guo, X. Adsorption Isotherm Models: Classification, Physical Meaning, Application and Solving Method. *Chemosphere* **2020**, *258*, 127279. [CrossRef]
25. Sips, R. On the Structure of a Catalyst Surface. *J. Chem. Phys.* **1948**, *16*, 490–495. [CrossRef]
26. Freundlich, H.M.F. Über Die Adsorption in Lösungen. *Z. Phys. Chem.* **1906**, *57*, 385–470. [CrossRef]
27. Langmuir, I. The Adsorption of Gases on Plane Surfaces of Glass, Mica and Platinum. *J. Am. Chem. Soc.* **1918**, *40*, 1361–1403. [CrossRef]
28. Al-Ghouti, M.A.; Da'ana, D.A. Guidelines for the Use and Interpretation of Adsorption Isotherm Models: A Review. *J. Hazard. Mater.* **2020**, *393*, 122383. [CrossRef] [PubMed]
29. Ciarlantini, C.; Francolini, I.; Silvestro, I.; Mariano, A.; Scotto d'Abusco, A.; Piozzi, A. Design of Bioactive and Biomimetic Scaffolds Based on Chitosan-Alginate Polyelectrolyte Complexes for Tissue Engineering. *Carbohydr. Polym.* **2024**, *327*, 121684. [CrossRef]
30. Tang, J.; Wang, L.; Qin, W.; Qing, Z.; Du, C.; Xiao, S.; Yan, B. High Reusability and Adsorption Capacity of Acid Washed Calcium Alginate/Chitosan Composite Hydrogel Spheres in the Removal of Norfloxacin. *Chemosphere* **2023**, *335*, 139048. [CrossRef]
31. Candia, C.; Gallardo-Moya, D.; Guerrero, J.; Leal, D.; Mansilla, A.; Martínez-Gómez, F.; Matsuhiro, B.; Yáñez-S, M. Characterization of Alginate from Antarctic Himantothallus Grandifolius (Phaeophyceae) and Preparation of Polyelectrolyte Complexes with Chitosan. *J. Appl. Polym. Sci.* **2023**, *140*, e54688. [CrossRef]
32. Steiger, B.G.K.; Wilson, L.D. Ternary Metal-Alginate-Chitosan Composites for Controlled Uptake of Methyl Orange. *Surfaces* **2022**, *5*, 429–444. [CrossRef]
33. Aguirre, J.M.; Gutiérrez, A.; Giraldo, O. Simple Route for the Synthesis of Copper Hydroxy Salts. *J. Braz. Chem. Soc.* **2011**, *22*, 546–551. [CrossRef]
34. Zotov, N.; Petrov, K.; Dimitrova-Pankova, M. Infrared Spectra of Cu(II)-Co(II) Mixed Hydroxide Nitrates. *J. Phys. Chem. Solids* **1990**, *51*, 1199–1205. [CrossRef]
35. Jackson, B.P.; Miller, W.P. Effectiveness of Phosphate and Hydroxide for Desorption of Arsenic and Selenium Species from Iron Oxides. *Soil Sci. Soc. Am. J.* **2000**, *64*, 1616–1622. [CrossRef]
36. Zeng, H.; Fisher, B.; Giammar, D.E. Individual and Competitive Adsorption of Arsenate and Phosphate To a High-Surface-Area Iron Oxide-Based Sorbent. *Environ. Sci. Technol.* **2008**, *42*, 147–152. [CrossRef]
37. Tchieda, V.K.; D'Amato, E.; Chiavola, A.; Parisi, M.; Chianese, A.; Amamra, M.; Kanaev, A. Removal of Arsenic by Alumina: Effects of Material Size, Additives, and Water Contaminants. *CLEAN—Soil Air Water* **2016**, *44*, 496–505. [CrossRef]
38. Martinson, C.A.; Reddy, K.J. Adsorption of Arsenic(III) and Arsenic(V) by Cupric Oxide Nanoparticles. *J. Colloid Interface Sci.* **2009**, *336*, 406–411. [CrossRef]
39. Elwakeel, K.Z.; Guibal, E. Arsenic(V) Sorption Using Chitosan/Cu(OH) 2 and Chitosan/CuO Composite Sorbents. *Carbohydr. Polym.* **2015**, *134*, 190–204. [CrossRef] [PubMed]
40. Ramesh, T.N.; Madhu, T.L. Thermal Decomposition Studies of Layered Metal Hydroxynitrates (Metal: Cu, Zn, Cu/Co, and Zn/Co). *Int. J. Inorg. Chem.* **2015**, *2015*, 536470. [CrossRef]
41. El Issmaeli, Y.; Lahrichi, A.; Kalanur, S.S.; Natarajan, S.K.; Pollet, B.G. Recent Advances and Prospects of FeOOH-Based Electrode Materials for Supercapacitors. *Batteries* **2023**, *9*, 259. [CrossRef]

Disclaimer/Publisher's Note: The statements, opinions and data contained in all publications are solely those of the individual author(s) and contributor(s) and not of MDPI and/or the editor(s). MDPI and/or the editor(s) disclaim responsibility for any injury to people or property resulting from any ideas, methods, instructions or products referred to in the content.